

# Deriving High-Resolution Reservoir Bathymetry From ICESat-2 Prototype Photon-Counting Lidar and Landsat Imagery

Yao Li<sup>1</sup>, Huilin Gao<sup>1</sup>, Senior Member, IEEE, Michael F. Jasinski, Shuai Zhang<sup>2</sup>, and Jeremy D. Stoll<sup>1</sup>

**Abstract**—Knowledge of reservoir bathymetry is essential for many studies on terrestrial hydrological and biogeochemical processes. However, there are currently no cost-effective approaches to derive reservoir bathymetry at the global scale. This study explores the potential of generating high-resolution global bathymetry using elevation data collected by the 532-nm Advanced Topographic Laser Altimeter System (ATLAS) onboard the Ice, Cloud, and Land Elevation Satellite (ICESat-2). The novel algorithm was developed and tested using the ICESat-2 airborne prototype, the Multiple Altimeter Beam Experimental Lidar (MABEL), with Landsat-based water classifications (from 1982 to 2017). MABEL photon elevations were paired with Landsat water occurrence percentiles to establish the elevation-area (E-A) relationship, which in turn was applied to the percentile image to obtain partial bathymetry over the historic dynamic range of reservoir area. The bathymetry for the central area was projected to achieve the full bathymetry. The bathymetry image was then embedded onto the digital elevation model (DEM). Results were validated over Lake Mead against survey data. Results over four transects show coefficient of determination ( $R^2$ ) values from 0.82 to 0.99 and root-mean-square error (RMSE) values from 1.18 to 2.36 m. In addition, the E-A and elevation-storage (E-S) curves have RMSEs of 1.56 m and 0.08 km<sup>3</sup>, respectively. Over the entire dynamic reservoir area, the derived bathymetry agrees very well with independent survey data, except for within the highest and lowest percentile bands. With abundant overpassing tracks and high spatial resolution, the newly launched ICESat-2 should enable the derivation of bathymetry over an unprecedented number of reservoirs.

Manuscript received June 28, 2018; revised October 15, 2018, March 15, 2019, and April 28, 2019; accepted May 10, 2019. This work was supported in part by the NASA Science of Terra, Aqua, and Suomi NPP (TASNPP) Program under Grant 80NSSC18K0939, in part by the ICESat-2 Project Office at the Goddard Space Flight Center, and in part by the ICESat-2 Early Adopter Program. (Corresponding author: Huilin Gao.)

Y. Li and H. Gao are with the Zachry Department of Civil and Environmental Engineering, Texas A&M University, College Station, TX 77843 USA (e-mail: liyao@tamu.edu; hgao@civil.tamu.edu).

M. F. Jasinski is with the Hydrological Sciences Laboratory, NASA Goddard Space Flight Center, Greenbelt, MD 20771 USA (e-mail: michael.f.jasinski@nasa.gov).

S. Zhang is with the Department of Geological Sciences, The University of North Carolina at Chapel Hill, Chapel Hill, NC 27514 USA (e-mail: tamuzhang@gmail.com).

J. D. Stoll is with the Hydrological Sciences Laboratory, NASA Goddard Space Flight Center, Greenbelt, MD 20771 USA, and also with Science Systems and Applications, Inc., Lanham, MD 20706 USA (e-mail: jeremy.d.stoll@nasa.gov).

Color versions of one or more of the figures in this paper are available online at <http://ieeexplore.ieee.org>.

Digital Object Identifier 10.1109/TGRS.2019.2917012

**Index Terms**—Ice, Cloud, and Land Elevation Satellite (ICESat-2), Landsat, Multiple Altimeter Beam Experimental Lidar (MABEL), reservoir bathymetry.

## I. INTRODUCTION

**K**NOWLEDGE of bathymetry (i.e., underwater topography) is critical for the understanding and accurate modeling of many lake, reservoir, and river processes, including surface water and energy exchanges, circulation, stream discharge, and biogeochemical cycles [1]–[3]. Lake bathymetries and their associated storage levels can significantly influence local and regional weather [4]–[6], despite lakes and reservoirs covering only 2.4% of all continents [7]. Although lake and reservoir models have been coupled to some weather models (such as the European Centre for Medium-Range Weather Forecasts' Integrated Forecasting System), to incorporate heat storage effects [8], lake and reservoir depth and surface area are treated as static due to the lack of bathymetry information. Considering the large variations of lake and reservoir extent (and therefore depth) [9], a more dynamic representation of lakes and reservoirs is required in weather forecast models. Furthermore, water retained by reservoirs has long-term impacts on the hydrological systems over most large river basins [10]–[13]. Although reservoirs have been explicitly represented in an increasing number of large-scale hydrological models and earth system models [14]–[18], the bathymetry in these models has virtually always been oversimplified. For instance, Hanasaki *et al.* [16] simulated reservoir release amount while assuming constant surface area. This directly inhibits the ability to simulate daily streamflow in a manner suitable for global flood forecasting [19]. Within individual reservoirs, bathymetry is a required input for hydrodynamic circulation and water quality models—which are used for supporting navigation, routing, dredging planning, and sedimentation analysis [20].

Despite its importance, spatially explicit knowledge of reservoir bathymetry (and the associated parameters) is crucially lacking at a global scale [21]. Bathymetry is typically mapped through surveys with echo-sounding equipment, airborne lidar, and optical imaging sensors [22]. The echo-sounding method is highly accurate but inefficient and expensive [23]. Airborne lidar using high-energy sensors can penetrate through relatively deep waters (up to tens of meters depending on the water clarity) with high accuracy [24], but it is relatively expensive

for rivers and limited by swath width [22], preventing its application at larger scales. Over the Alaska North Slope, Saylam *et al.* [25] used airborne lidar to map the bathymetry of thousands of small shallow lakes. While more cost-effective for lakes and reservoirs, optical sensing is limited by water depth and optical properties [26]. It further requires simultaneous *in situ* observations, whose spatial distributions and reliability affect bathymetric accuracy. More recently, some global data sets have emerged that use alternative approaches to infer lake and reservoir geometry information, but they are insufficient for providing high-resolution 3-D bathymetry data that are locally practical. For instance, lake bathymetry information derived from the ETOPO1 Global Relief Model [27] has been used in climate modeling [28], but it is only applicable to large lakes and reservoirs (e.g., the Great Lakes) due to its coarse resolution (1 arc-minute). Yigzaw *et al.* [29] developed a global storage-area-depth data set that used an optimal geometric shape for each reservoir—but this data set does not provide the 3-D bathymetry information. Tseng *et al.* [30] projected the underwater slope using the digital elevation model (DEM) data above the water surface and combined this approximated bathymetry with Landsat area to estimate water elevation variations at the Hoover Dam. Although the resultant water surface height was verified by *in situ* data, the accuracy of their projected bathymetry was not directly evaluated. Both HydroLAKES [21] and the Global Reservoir and Dam database (GRanD) [11] only provide the mean depth of reservoirs—which is inadequate to generate storage-area-depth relationships. Indeed, the bathymetry problem is essentially an elevation measurement problem. The fast growth of spaceborne radar altimetry has potential use for deriving reservoir bathymetry, though current studies are mainly focused on the derivation of the area-volume-elevation relationships [31]–[33]. More recently, Getirana *et al.* [34] combined the time-series radar altimetry and Landsat data to derive the 3-D bathymetry of the lower portion of Lake Mead. This method is potentially applicable only to large bodies where elevation observations from radar altimeters are available [35].

Thus, the objective of this study is to explore the potential of generating high-resolution reservoir bathymetry at a global scale using the data collected by the photon-counting lidar onboard the new Ice, Cloud, and Land Elevation Satellite (ICESat-2). As the first satellite laser ranging altimeter, ICE-Sat collected elevation data with an approximately 70-m footprint and 170-m along track spacing, which has been widely used for measuring lake and reservoir levels [36], [37] and calculating the elevation-area (E-A) relationship [38]. ICESat-2 decreases the footprint and along-track spacing to 17 and 0.7 m, respectively, thereby improving its capability to obtain high-quality bathymetric information. Recent analysis of airborne Multiple Altimeter Beam Experimental Lidar (MABEL) observations over several inland water bodies indicates that ICESat-2 can penetrate the water to more than 10 m, depending on water quality [39]. In this study, a novel algorithm is developed to derive bathymetry by combining one transect of MABEL airborne elevation data with historic series Landsat image classifications. As the prototype of the

TABLE I  
SPECIFICATION OF LANDSAT IMAGES USED TO GENERATE THE WATER OCCURRENCE PERCENTILE IMAGE

Satellite	Sensor	Band	Period	Number
Landsat-4	TM	NIR (760 nm - 900 nm)	1982-1992	6
Landsat-5	TM	NIR (760 nm - 900 nm)	1984-2011	293
Landsat-7	ETM+	NIR (770 nm - 900 nm)	1999-2003	63
Landsat-8	OLI	NIR (851 nm - 859 nm)	2013-2017	48

Advanced Topographic Laser Altimeter System (ATLAS) on ICESat-2, MABEL can retrieve surface elevation values with a mean precision of approximately 5–7 cm [39]. By relating the MABEL data to the water occurrence percentile image from Landsat, the 3-D bathymetry can be derived. With the launch of ICESat-2 in September 2018, this algorithm holds great promise for generating bathymetry for global reservoirs with areas as small as several square kilometers.

## II. DATA AND METHODS

### A. Data

The generation of the bathymetry results in this study relied on information from two data sources: Landsat and MABEL. From 1982 to 2017, Landsat Thematic Mapper (TM), Enhanced Thematic Mapper Plus (ETM+), and Operational Land Imager (OLI) images (at a spatial resolution of 30 m) were obtained from the United States Geological Survey (USGS) (<https://earthexplorer.usgs.gov/>). A total of 410 high-quality images, completely free of cloud contamination, were collected over the Lake Mead area (Table I).

MABEL elevation data were collected over Lake Mead on February 24, 2012, with reported clear sky conditions and a relatively low water turbidity of 1.6 NTU [39]. The flight overpassed the western part of Lake Mead in a Southwest to Northeast direction [Fig. 1(a)]. MABEL collected data over a ~2-m footprint along its track using the same 532-nm photon counting lidar as ATLAS. Fig. 1(b) shows the profile of the MABEL track, with the red dots indicating the samples used (in this study) to establish the E-A relationship. The information from the captured photons was then processed to generate an elevation data set with an average segment length of 50 m. Because the original MABEL data were referenced to the WGS84 ellipsoid datum, they were converted to the EGM96 geoid so that the final bathymetry could be merged with the Shuttle Radar Topography Mission (SRTM) DEM data properly. Given a specific location, the EGM96 geoid height (N) can be calculated using the latitude and longitude information via the online tool provided by the National Geospatial-Intelligence Agency Office of Geomatics (<http://earth-info.nga.mil/GandG/wgs84/gravitymod/egm96/intpt.html>). Then, the orthometric height with respect to the EGM96 geoid (H) (at the given location) can be calculated as the difference between the WGS84 ellipsoid height h (i.e., MABEL reported elevation) and the EGM96 geoid height (N).

The SRTM 1 arc-second (~30 m) elevation data were obtained from the USGS EarthExplorer website (<https://earthexplorer.usgs.gov/>). As the first near-global

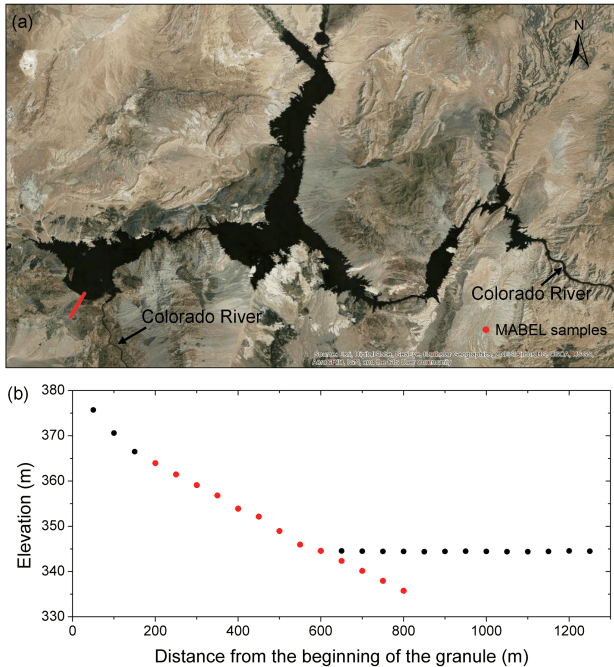


Fig. 1. (a) Location map and (b) elevation profile of the MABEL samples. The points in (b) represent the samples collected by MABEL. Those in red are the samples used in this study to establish the E-A relationship.

high-resolution DEM (from 56° S to 60° N), the SRTM data set has been widely used in various research fields (including geology, geomorphology, glaciology, and hydrology) [40]–[42]. However, because the radar signal cannot penetrate through the water—and because the SRTM data were only collected once—reservoir bathymetry information below the water level at the SRTM acquisition time cannot be accessed. More recently, Yamazaki *et al.* [43] developed a high-accuracy global DEM database with 3 arc-second ( $\sim 90$  m) resolution. Still, this data set cannot provide elevation information below the water surface.

The Lake Mead lidar survey data collected by the United States Bureau of Reclamation (USBR) in 2009 [44] were used to validate the part of the bathymetry product which was generated using MABEL data. This data set provides detailed elevation contour values for the emergent shoreline areas of Lake Mead, and it covers an area of 445.48 km<sup>2</sup> with elevation values ranging from 334.06 m (1096 ft) to 374.90 m (1230 ft) at a 0.61 m (2 ft) interval. For validation purposes, the lidar contours were converted to elevation point values and then resampled to the bathymetry values at a resolution of 30 m using the inverse distance weighted (IDW) interpolation method to match the resolution of the resultant bathymetry. In addition, the contour data—with an elevation interval of 10 m, collected by the 2001 sedimentation survey—were used to validate the projected portion of the bathymetry.

## B. Methods

This reservoir bathymetry generation algorithm contains three main steps (Fig. 2). First, a water occurrence percentile image was generated for Lake Mead using Landsat image

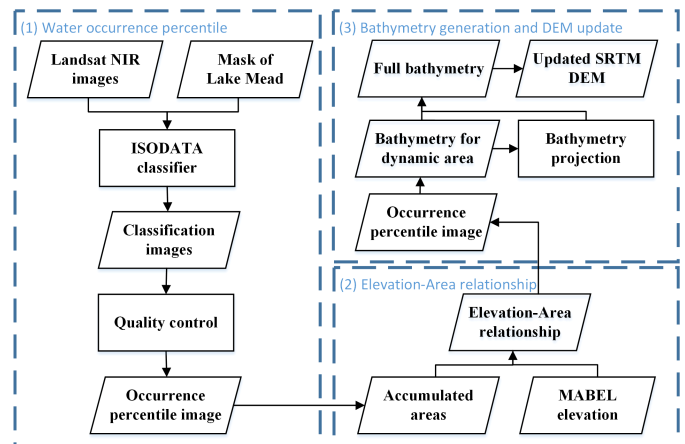


Fig. 2. Flowchart of the bathymetry generation algorithm. It consists of three parts (separated by the blue boxes): 1) the water occurrence percentile image was generated from the Landsat classifications, which essentially provided the bathymetry contours; 2) the E-A relationship was established by combining the area from the occurrence percentile image with MABEL elevation values. This was then used to identify and assign elevation values to the contours; and 3) the E-A relationship was applied to the percentile image to obtain the bathymetry for the dynamic lake area—which was then used to project the bathymetry for the central area to obtain the full lake bathymetry. Then, the full bathymetry was overlapped with the SRTM DEM data to replace the constant value.

classifications over the reservoir's historic dynamic elevation variation range. The occurrence percentile essentially provides the bathymetry contours over the reservoir dynamic area. Second, MABEL elevation data were paired up with the water occurrence percentile image to establish the E-A relationship, which was then used to identify and assign elevation values to the contours. Third, the E-A relationship was applied to the percentile image to obtain the bathymetry for the dynamic reservoir area—which was then used to project the bathymetry for the central area. The full bathymetry was then embedded onto the SRTM data to replace the constant DEM value.

**1) Water Occurrence Percentile:** The water occurrence percentile image shows the frequency at which each pixel is classified as water, which is calculated as the ratio of the time classified as water versus the total observation time. The percentile image can characterize the elevation gradients and act as the base map of the bathymetry [45].

To obtain the water occurrence percentile image, the water classifications were first conducted by applying the Iterative Self-Organizing Data Analysis Techniques Algorithm (ISODATA) [46], [47] to the 410 Landsat near-infrared (NIR) images collected over Lake Mead from 1982 to 2017. NIR was selected because it is strongly absorbed by water but barely absorbed by terrestrial vegetation and dry soil [48]. Compared to the methods that involve using water indexes—such as the normalized difference water index (NDWI) [48]—the unsupervised ISODATA technique has the advantage of producing consistent water classifications without having to choose a threshold based on the water body and season [49], [50]. To reduce the computation cost and enhance the classification accuracy, a mask was constructed by buffering 10 km of the Lake Mead shapefile. The classification process was performed within the masked

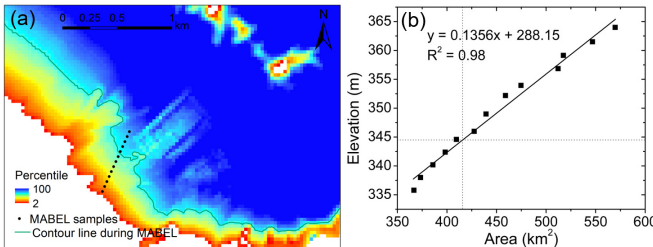


Fig. 3. (a) Locations of the MABEL samples and (b) E-A relationship of Lake Mead.

area of each image. However, some of the Landsat images were also contaminated by mountain shadows. Lake Mead is partly surrounded by mountain ranges, such as the River Mountains and the Muddy Mountains (the portion within the Boulder Basin). Due to the effect of satellite incident angle, mountain shadows may appear in some images—and these images are very likely to be misclassified as water bodies. To correct this, any water pixel in the water classification image which had an elevation value greater than 400 m was reclassified as land. A water occurrence percentile image was then created for Lake Mead. To reduce the impacts of random errors, pixels with occurrence values less than 1% were removed from the percentile image.

2) *Elevation–Area Relationship*: The E–A relationship is an essential element of the bathymetry retrieval algorithm. E–A relationships vary with water body and have been used as the key function for calculating storage values from either surface area values or elevation values [32], [33], [51]. To derive the E–A relationship for Lake Mead, MABEL elevation points were projected onto the occurrence percentile image, with each point corresponding to a specific percentile value—each of which could be regarded as a contour. The corresponding water area within that specific contour was then calculated. As shown in [39], MABEL photons penetrated the water body to about 9.2 m of depth. These elevation measurements (below the water surface) were also paired up with the occurrence percentile image, which allowed for four more samples for deriving the E–A relationship [Fig. 1(b)]. Fig. 3 suggests that the resulting Lake Mead E–A relationship is very robust (with an  $R^2$  value of 0.98).

3) *Bathymetry Generation and SRTM DEM Update*: The elevation at each percentile contour was determined by applying the E–A relationship to the area enclosed by that contour. Because the water occurrence percentile image is based on 35 years of Landsat classifications, this procedure led to a full dynamic range of bathymetry values. For the central reservoir area, the Tseng *et al.* [30] algorithm was adopted to project the part of bathymetry not accessible by MABEL and Landsat. In [30], an algorithm was developed to extend the part of Lake Mead bathymetry not measured by SRTM DEM using the elevation information of the surrounding land area. They projected the bathymetry with an elevation range from 320 to 372 m. In this study, we applied the Tseng *et al.* [30] algorithm to extrapolate our remotely sensed partial bathymetry (from MABEL and Landsat) into a bathymetry containing the central reservoir area. We modified the Tseng *et al.* [30] algorithm

by utilizing the storage capacity information to determine the reservoir bottom level. The cumulative storage associated with the bathymetry was estimated using the following equation:

$$V_n = \sum_{i=1}^{n-1} \frac{(h_{i+1} - h_i)(A_{i+1} + A_i)}{2} \quad (1)$$

where  $n$  is the number of contours. The storage at capacity ( $V_c$ ) and elevation at capacity ( $h_c$ ) were obtained from surveying data provided by the USBR, and the area at capacity ( $A_c$ ) was obtained by applying  $h_c$  to the E–A relationship.  $A_i$  is the entire water surface area enclosed by the  $i$ th contour, which corresponds to the elevation  $h_i$ . Thus, the storage value corresponding to each contour was obtained. At the end of each projection step, we calculated the cumulative storage from all contours. When the cumulative storage reached the reservoir capacity, the projection of bathymetry was terminated.

By combining the remotely sensed and projected bathymetry, the full bathymetry was obtained. This was then embedded onto the SRTM DEM data set to replace the constant value. We calculated the elevation value associated with the reservoir area that corresponded to the constant DEM value using the MABEL-based E–A relationship. Then, the elevation difference between this elevation value and the constant DEM value was used to correct the bathymetry data. It is worth noting that our bathymetry data have higher accuracy than the DEM data, and the purpose of the correction is simply to keep the DEM data consistent.

4) *Validation Scheme*: This study used the USBR lidar survey and sedimentation survey data sets to validate the bathymetry product. The lidar survey—which is of high resolution and quality but only available along the coast—was adopted for evaluating the part of bathymetry directly derived from remotely sensed data. First, four transects from the North, South, West, and East regions were selected across the shorelines of Lake Mead. The elevations of these transects from this study were compared with their counterparts from lidar. To further evaluate the performance of the remotely sensed bathymetry over the entire reservoir, we divided the percentile image into ten bands (at a 10% increment) and compared the elevation statistics within each band (i.e., we compared the mean and standard deviation). This can better scrutinize which parts (higher or lower elevation zones) tend to have larger/smaller errors (e.g., standard deviations and overestimations versus underestimations). It should be noted that the evaluated variable is the elevation, not the percentile. In addition, indirect validations were conducted over the full bathymetry by comparing our results for the E–A and elevation–storage (E–S) relationships with their counterparts from the lidar and sedimentation survey datasets. The E–A and E–S relationships based on lidar and sedimentation data were provided by the USBR [44], [52]. Equation (1) is used to calculate the storage from the bathymetry data, from which the E–S relationship can be derived.

The sedimentation data were primarily used for evaluating the projected part of the bathymetry. Because the contour data provided by the USBR (with an elevation interval

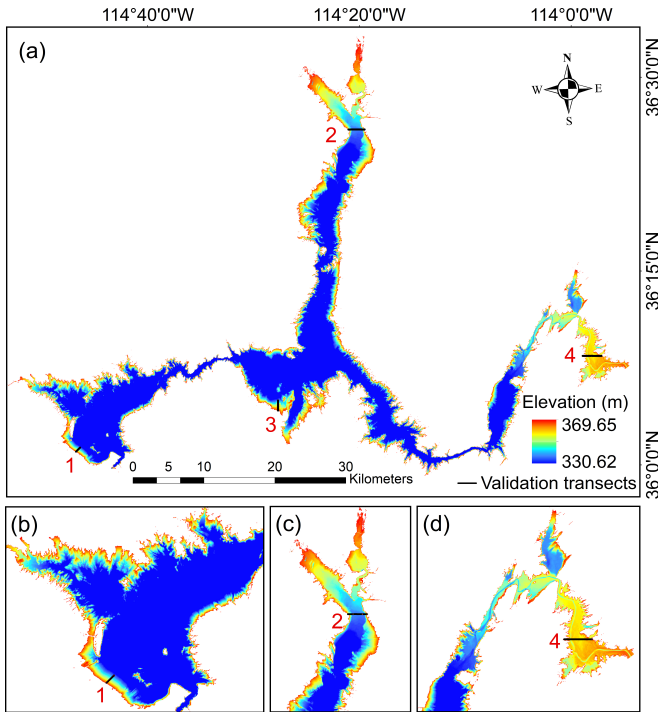


Fig. 4. Remotely sensed bathymetry of Lake Mead. (a) Overall bathymetry. (b)–(d) Close-up views of three subregions: (b) West, (c) North, and (d) East. The transects labeled 1–4 consist of points which were used for validation purposes.

of 10 m) are not continuous, it is difficult to directly use this data set to validate the bathymetry values. Thus, we first visually compared the contours generated from the projected bathymetry with the survey contours. Although the bathymetry contours from the sedimentation survey are fragmental, USBR did provide a look-up table detailing the E-A and E-S relationships [44], [52]. Thus, we compared these reported relationships with those from this study to quantify the overall performance of the projected bathymetry.

### III. RESULTS

#### A. Bathymetry Results

For the remotely sensed bathymetry values, the elevation range is from 330.62 to 369.65 m, which corresponds to a water surface area from 313.20 (inner zone) to 601.05 km<sup>2</sup> (outer zone), representing 58% of the reservoir capacity. When the SRTM DEM data were collected in February 2000, the reservoir area was about 587.50 km<sup>2</sup> with a constant elevation value, which means that no bathymetry information was acquired below the water surface. In comparison, our remotely sensed results can provide additional reservoir bathymetry information associated with an additional 274.30 km<sup>2</sup> (47%) of the reservoir area.

The remotely sensed bathymetry (for the entire reservoir area, with three subregions zoomed in upon) is shown in Fig. 4. Overall, the bathymetry has evident gradients, which are in agreement with the surrounding terrain of Lake Mead. For the western region [Fig. 4(b)], the bathymetry has steep elevation gradients across the shorelines, and the shapes of islands

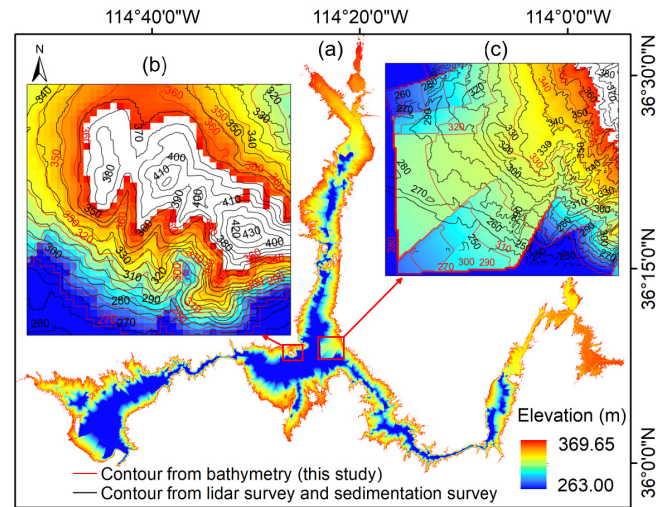


Fig. 5. (a) Full bathymetry of Lake Mead, including the remotely sensed bathymetry (330.62–369.65 m) and the projected bathymetry (263.00–330.62 m). (b), (c) Close-up views of two regions with (b) satisfactory and (c) unsatisfactory performances are selected to show the details. Note that the contour data from both sources have an elevation interval of 10 m. The contour data are not shown in (a) because they are relatively dense and would not be useful to the reader.

within this area are clearly captured. For the northern region [Fig. 4(c)], the gradients are gradual, indicating that this part of the reservoir is relatively flat as compared to the western part. As shown in Fig. 4(d), the topography near the Colorado River has been clearly captured.

Based on the Tseng *et al.* [30] method, we projected the bathymetry for the central area, which ranges from 263.00 to 330.62 m. The lowest elevation value (263.00 m) was determined by using the storage information calculated after (1). We calculated the storage for each contour layer (from outer to inner) and accumulated them. When the elevation is at 263.00 m, the accumulated storage reached the capacity value and we thus ended the projection. Fig. 5(a) shows the full bathymetry of Lake Mead, including the remotely sensed part (330.62–369.65 m) and the projected part (263.00–330.62 m). Although the performance of the projected bathymetry varies with region, it has an overall good pattern. Close-up views of two regions were selected to show the details. In the subset area shown in Fig. 5(b), the contours based on the projected bathymetry agree well with those from the sedimentation survey data. However, in the subdomain depicted by Fig. 5(c), the projected results largely missed those from the survey—which was caused by the assumption made in [30] that the slope remains constant. The resultant full bathymetry was then embedded onto the SRTM DEM data. The comparison between the bathymetry and SRTM DEM is shown in Fig. 6. It is evident that the elevation of Lake Mead from DEM is constant (372 m) over the entire reservoir. In order to be accurate, we first applied the reservoir area from the DEM (587.50 km<sup>2</sup>) to the MABEL-based E-A relationship to estimate its corresponding elevation (367.82 m). A systematic bias of 4.18 m was found between this elevation value and that according to the SRTM DEM. A bias correction of 4.18 m was

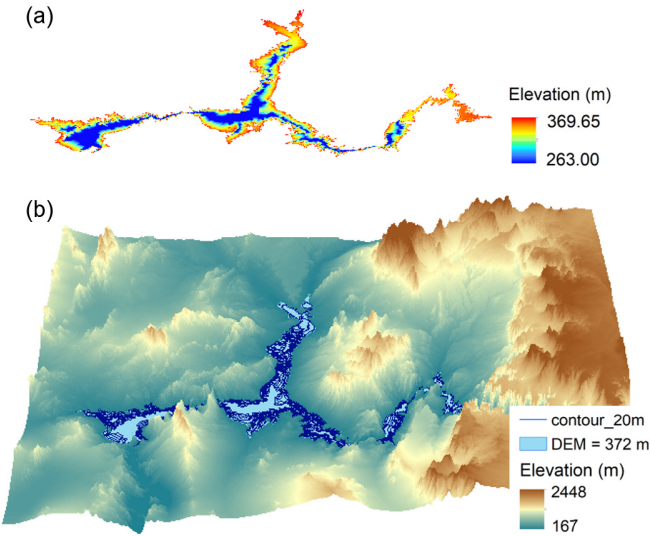


Fig. 6. (a) Full bathymetry and (b) SRTM DEM data over Lake Mead. The contour map (with a 20-m interval) is derived from the bathymetry information, and the DEM elevation is constant (372 m) over the entire lake.

then applied to the bathymetry such it could be seamlessly combined with the DEM. Thus, the part of the DEM with a constant value of 372 m was replaced by the part of the bathymetry results representing 372 m and below (after the systematic bias correction). Moreover, contour maps with different horizontal intervals (e.g., 5, 10, and 20 m) were drawn from the bathymetry, which can help to delineate the profile. An example of the contour map at a 20-m interval is shown in Fig. 6.

### B. Validation of the Bathymetry

The remotely sensed bathymetry product was validated using survey lidar data by comparing elevation values over selected transects and over the entire reservoir (by percentile band). Moreover, the full bathymetry was indirectly validated by comparing the E–A and E–S curves from this study with those derived from the surveys.

First, for the remotely sensed bathymetry, the elevations at four representative transects [whose locations are shown in Fig. 4(a)] were evaluated. The elevation profiles and scatterplots for these four transects using the data from this study (and the lidar data) are shown in Figs. 7 and 8, respectively. The estimated elevations show good correlation with those from the lidar survey, with  $R^2$  values of 0.99, 0.99, 0.98, and 0.82 for transects 1–4, respectively. The corresponding root-mean-square error (RMSE) values are 2.36, 1.18, 2.35, and 1.54 m. The statistical results of these four transects are shown in Table II. In addition, the Colorado River bottom can be clearly observed from the east transect profile [Fig. 7(d)]. In contrast, the river bottom according to the lidar measurements appeared to be flat. The three outliers appearing in Fig. 8(d) are due to the disagreement over the Colorado bottom, which leads to the relatively low  $R^2$  for this transect. Overall, the results indicate that the bathymetry product has relatively high accuracy.

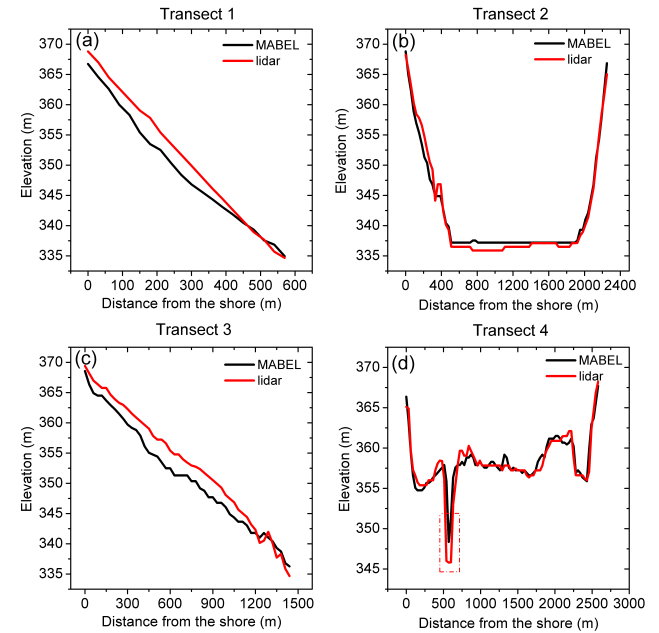


Fig. 7. Elevation profiles for the four validation transects. (a) Transect 1 as shown in Fig. 4, in the West part of Lake Mead, from Southwest to Northeast. (b) Transect 2 as shown in Fig. 4, in the North part of Lake Mead, from West to East. (c) Transect 3 as shown in Fig. 4, in the South part of Lake Mead, from South to North. (d) Transect 4 as shown in Fig. 4, in the East part of Lake Mead, from West to East.

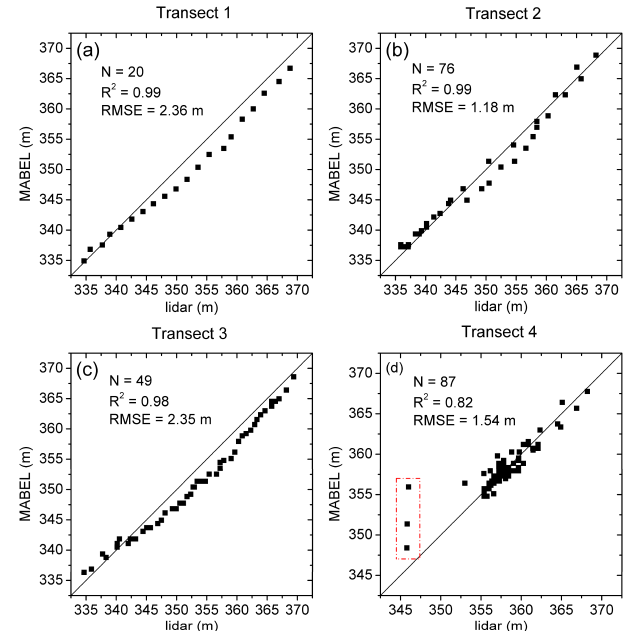


Fig. 8. Scatterplots of the four validation transects. (a) Transect 1 as shown in Fig. 4, in the West part of Lake Mead, from Southwest to Northeast. (b) Transect 2 as shown in Fig. 4, in the North part of Lake Mead, from West to East. (c) Transect 3 as shown in Fig. 4, in the South part of Lake Mead, from South to North. (d) Transect 4 as shown in Fig. 4, in the East part of Lake Mead, from West to East.

Fig. 9 compares the statistical bathymetry results obtained from this study with those obtained from the lidar survey within each percentile band (at a 10% interval). Although there is a clear overestimation in the 1%–30% range and an underestimation in the 80%–100% range, the derived bathymetry

TABLE II  
STATISTICAL RESULTS OF THE MABEL AND LIDAR ELEVATION VALUES FOR THE VALIDATION TRANSECTS

Transect	Elevation data	Max (m)	Min (m)	Mean (m)	SD (m)	N	R <sup>2</sup>	RMSE (m)	P-value
1	MABEL	366.73	334.95	349.17	9.71	20	0.99	2.36	$4.62 \times 10^{-19}$
	lidar	368.81	334.67	351.02	10.77				
2	MABEL	368.86	337.24	342.23	8.46	76	0.99	1.18	$7.49 \times 10^{-72}$
	lidar	368.24	335.89	341.96	9.05				
3	MABEL	368.60	336.31	351.30	8.75	49	0.98	2.35	$2.95 \times 10^{-42}$
	lidar	369.42	334.67	353.17	9.48				
4	MABEL	367.75	348.40	358.27	2.80	87	0.82	1.54	$6.82 \times 10^{-33}$
	lidar	368.24	345.79	358.03	3.48				

SD represents the standard deviation. The R<sup>2</sup> value and the P-value were derived from the Pearson correlation significance test.

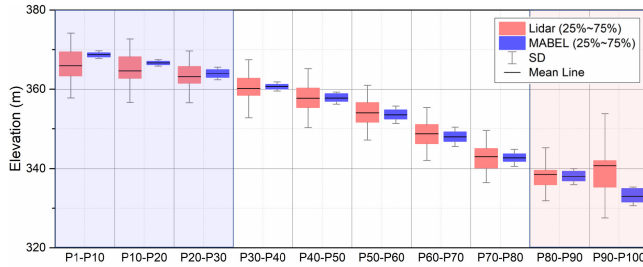


Fig. 9. Comparisons of the statistical results of the elevations within each percentile band (at a 10% interval) over the entire dynamic lake area. For the 1%–30% range, the mean elevation is overestimated by MABEL, whereas it is underestimated for the 80%–100% range.

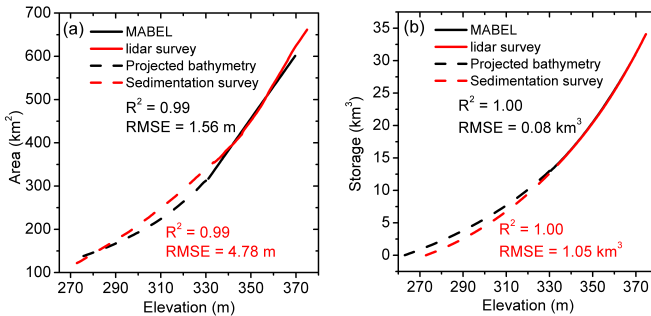


Fig. 10. Comparison of (a) the E-A relationship and (b) the E-S relationship for Lake Mead. The MABEL-based E-A and E-S relationships were compared with those from the lidar survey (with statistical values labeled in black), and the E-A and E-S relationships derived from the projected bathymetry were compared with those from the sedimentation survey (with statistical values labeled in red).

overall agrees very well with the lidar survey data. The survey data show a larger variation within each band, which can be attributed to both the higher resolution and the measurement error of the raw data. However, it is unclear why the survey elevations in the 90%–100% band are higher than those in the 80%–90% band.

In addition, we also quantified the uncertainties of the remotely sensed bathymetry. Since the penetration depth of MABEL elevation measurements depends on the water conditions, we changed the number of underwater pairs used in the E-A relationship and calculated the uncertainties of the retrieved elevations. The resultant uncertainties are from -1.39 (when the penetration depth was 9.2 m) to 1.30 m (when the penetration depth was 0 m), showing that our results are reliable.

Second, the E-A relationship—the critical factor affecting the reliability and accuracy of the bathymetry data—was

examined to indirectly validate the product. Although the MABEL-based E-A relationship appears to be more linear than the one from lidar, it has shown good overall consistency with the latter (with an R<sup>2</sup> of 0.99 and an RMSE of 1.56 m) [Fig. 10(a)]. With regard to the E-A relationship from the projected bathymetry, although it has a good correlation with the E-A relationship from the sedimentation survey data ( $R^2 = 0.99$ ), the vertical bias is relatively large (RMSE = 4.78 m). The survey reservoir storage values at each contour elevation were also utilized in the validation. Based on the elevation values and their corresponding areas from the bathymetry, the storage values can be calculated using (1). Fig. 10(b) shows the E-S curves derived from the bathymetry and the survey lidar and sedimentation data. By comparing the E-S relationships between remotely sensed bathymetry and lidar survey data (with an R<sup>2</sup> of 1.00 and an RMSE of 0.08 km<sup>3</sup>), it is evident that they are in very good agreement. Whereas for the comparison of the E-S relationships between the projected bathymetry and the sedimentation survey data, they have a good consistency ( $R^2 = 1.00$ ) but a large vertical mismatch (RMSE = 1.05 km<sup>3</sup>).

#### IV. DISCUSSION AND CONCLUSION

Although ICESat-2 is a follow-on mission to ICESat, it differs from its predecessor in its reliance only on the 532-nm wavelength and photon-counting detector technology. These two features allow for both light penetration into the subsurface and the high spatial resolution required for bathymetric sampling. The analysis of MABEL data in the current Lake Mead test case is thus not only representative of ICESat-2, but also any future satellite lidar possessing a 532-nm wavelength with photon-counting technology.

This study is the first attempt to improve the process of measuring reservoir bathymetry using ICESat-2 data and has the potential of generating bathymetry for global reservoirs when ICESat-2 ATLAS data become available. With high vertical precision (5–10 cm per 100 m segment length), a small along-track sampling interval (0.7 m), a small footprint diameter (17 m), and narrow horizontal track spacing (three sets of beam pairs; 90 m between each neighboring pair, 3 km between each pair set) [53], ATLAS is expected to capture the topography around numerous inland water bodies with areas as small as a few tenths of a square kilometer. Fig. 11 shows the ICESat-2 ground tracks over selected regions during two years. Over the Tibetan Plateau, even the smallest lake (0.4 km<sup>2</sup>) reported by HydroLAKES—a global digital map database for

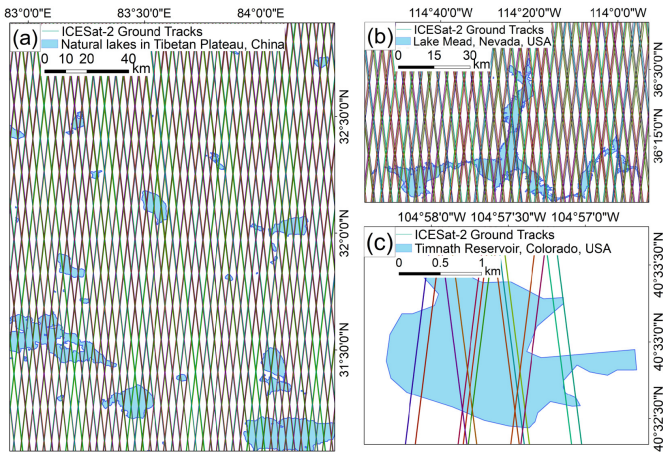


Fig. 11. ICESat-2 ground tracks for (a) some natural lakes in the Tibetan Plateau, China ( $0.4 \text{ km}^2 < \text{area} < 498.06 \text{ km}^2$ ). (b) Lake Mead, NV, USA (area =  $580.95 \text{ km}^2$ ). (c) Timnath Reservoir, CO, USA (area =  $2.33 \text{ km}^2$ ). The line colors represent different tracks from different passes. ICESat-2 ground tracks were downloaded from <https://icesat-2.gsfc.nasa.gov/science/specs>.

lakes with surface areas greater than 10 ha—would have four overpasses. For lakes and reservoirs larger than  $1 \text{ km}^2$ , there are usually multiple tracks (for instance, there are 14 tracks over the Timnath Reservoir). A total of 423 tracks are found in two years for Lake Mead, as compared to 52 ICESat overpasses (from 2003 to 2009) and 119 radar altimeter overpasses (with five satellite radar sensors considered from 2000 to 2014). Particularly, the spatial resolution and vertical precision of ICESat-2 are significantly better than those of ICESat and radar altimeters. Thus, ICESat-2 has a unique advantage for reducing the errors and uncertainties of the future bathymetry product.

Previous studies have shown that the photon-counting MABEL system can profile the subsurface light attenuation—depending on pulse strength, water clarity, and atmospheric conditions—down to about one Secchi disc depth (SDD) under clear skies [39]. The 2012 experiment over Lake Mead, which exhibited low turbidity of 1.6 NTU, was flown during clear night skies with low backscatter, resulting in a penetration of 9.2 m. Other water bodies with higher turbidity and less favorable meteorological conditions would exhibit less penetration. As shown in this study, the underwater elevation samples collected by MABEL provide an added value to improve the elevation range of the resulted bathymetry (through a more accurate E–A relationship). It is true that the water clarity may not be ideal during every ICESat-2 overpass—and for some reservoirs, the water clarity is always low. However, for the reservoirs where the laser cannot reach significant depth, the samples across the shoreline area can provide extra data points (because of the high spatial resolution of ICESat-2). For instance, the three highest points in Fig. 1(b) actually are within/near Lake Mead’s elevation at capacity, even though the percentile image did not cover them (since none of the 410 selected Landsat images were collected when the reservoir level was the highest). Furthermore, during the three-year expected operational life of ICESat-2, we will be able to obtain elevation values from multiple tracks.

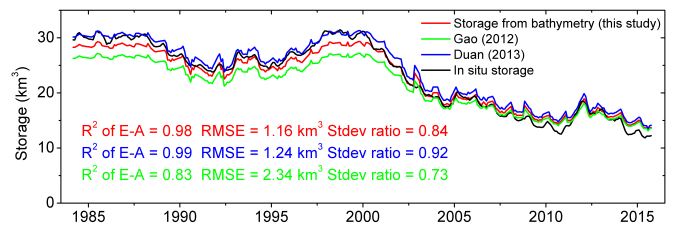


Fig. 12. Storage estimations of Lake Mead from 1984 to 2015 using different E–A relationships. The time-series surface area of Lake Mead was provided by Zhao and Gao [45].

The minimum elevation to be sampled by each ICESat-2 track depends on both the penetration depth and the water surface level. Because water surface level varies both seasonally and interannually, a good range of nearshore elevation values can be collected from multiple tracks passing over a given reservoir—even for reservoirs with low clarity (penetration). Even if the ICESat-2 observations cannot cover the entire dynamic area of a given reservoir, an extrapolation of the derived E–A relationship using the contour area values of the percentile image (from 35 years of Landsat imagery covering a large range of area dynamics) will lead to a good representation of the reservoir bathymetry. Such bathymetry results can satisfy the demands of most applications (such as hydrologic modeling and reservoir management).

The projected bathymetry results have relatively large uncertainties because this method assumes that the underwater slope remains constant. The method linearly extrapolates the slope of the boundary, which was derived from the nearby grids ( $3 \times 3$  window). Therefore, the quality of the data (i.e., the elevation within the 90%–100% percentile) used to calculate the slope determines the performance of the projection. Although the projected bathymetry is not as robust as the remotely sensed bathymetry, it bridges the gap for the area far off the coast and helps to achieve the full bathymetry. The accuracy and uncertainties of the detected reservoir bottom depend on several factors. The first of these involves the errors and uncertainties associated with the capacity values of elevation and storage—which can directly result in biased bottom estimations. The second factor involves the E–A and E–S relationships in both the dynamic portion and the extrapolated portion. On the one hand, the extrapolated portion tends to have much larger elevation errors due to the simplified assumption of constant slope. On the other hand, for the same elevation interval, the extrapolated portion is associated with a much smaller volume than that from the upper dynamic part. In this study, because the capacity values were adopted from the USBR, the E–A and E–S relationships performed reasonably well in the dynamic portion (Fig. 10). Furthermore, the bottom elevation derived from this study (263.0 m) is close to that measured through the sedimentation survey (272.8 m).

The photon-counting lidar-based bathymetry product also leads to high-quality E–A relationships, which will contribute to more accurate estimations of reservoir storage variations (when applied to either satellite imagery or altimetry data). Many studies suggest that the  $R^2$  of the E–A relationship directly affects the performance of the corresponding remotely

sensed reservoir storage estimation [35], [38], [54]. A set of comparisons—all using the same Landsat water areas from [45], but different E–A relationships (for Lake Mead)—clearly demonstrate the benefit of accurate elevation measurements (Fig. 12). We used the RMSE and the standard deviation ratio (Stdev ratio)—the ratio between the standard deviations of estimated and *in situ* reservoir storage time series—to evaluate the storage estimations. By combining radar altimetry data with MODIS-based area estimates, the E–A relationship from [51] has the lowest  $R^2$  value (0.83) and the largest storage estimation error (RMSE = 2.34 km<sup>3</sup> and Stdev ratio = 0.73). The poor E–A relationship is mainly attributed to the low resolution of MODIS (250 m). By substituting MODIS with Landsat, the  $R^2$  value of the E–A relationship from [55] was improved to 0.99, which leads to better storage results (RMSE = 1.24 km<sup>3</sup> and Stdev ratio = 0.92). With elevation values obtained from the photon counting lidar, the storage error was further reduced (RMSE = 1.16 km<sup>3</sup>) and the Stdev ratio decreased to 0.84. Since the E–A relationships have different slopes and intercepts, each one has its own best-fit spectrum with the *in situ* E–A relationship. Even for the storage estimations using the least accurate E–A relationship from [51], there is still very good agreement with the *in situ* observations when the area values are within a certain range. This can explain why the performances of the E–A relationships vary with the area values when estimating the storage values. Unlike the other two algorithms—which relied on radar altimetry data collected over multiple years—this algorithm leveraged elevations collected from just a single lidar track. Using data from multiple ICESat-2 tracks, this algorithm can perform even better.

More recently, Getirana *et al.* [34] derived the bathymetry for the lower portion of Lake Mead. A new contribution they made was to evaluate results from a suite of experiments. For the best performing one, they linearly interpolated the radar altimetry data (from 2002 to 2015) and then paired it up with the Landsat based water extent to obtain the bathymetry (with an elevation range of 23.90 m). By incorporating the gauge-based water levels (from 1983 to 2016), they improved the elevation range to 42.3 m. In comparison, our method generated the dynamic bathymetry at an elevation range of 39.03 m, solely based on remote sensing data (through overlaying a single, high-quality lidar track over the Landsat water occurrence image). To terminate the bathymetry extrapolation, Getirana *et al.* [34] used the *in situ* downstream riverbed elevation, while we used the reservoir storage capacity. The use of *in situ* riverbed elevation values may be limited by data availability, but reservoir capacity values can be obtained from the GRanD database [11]. Furthermore, by embedding the bathymetry onto the SRTM DEM data set, results from this study may be used to support the mapping and modeling of flood inundation in the vicinity of the reservoir [56].

This algorithm still has some limitations that need to be addressed. For example, even though the remotely sensed algorithm leverages 35 years of Landsat information to characterize the largest range of reservoir bathymetry values, it is impossible to derive the bathymetry of the very central area that is covered by water all of the time. Known as the “inactive

pool,” this bottom portion of a reservoir is intended for functions such as sedimentation containment and ecosystem protection [57]. Because we projected the bathymetry for the central area to represent the full reservoir, its quality may not satisfy the applications that need high-quality elevations (e.g., navigation). Another concern is the existence of the mountain shadow. Many reservoirs are located in mountainous regions, and areas covered by shadows can be easily misclassified as water. Although DEM data can help eliminate the mountain shadow within the masked area, shadows near the boundary can still have a minor impact on the classification result.

In summary, we demonstrate that the 532 nm MABEL elevations and imagery data sets can be combined to generate high-resolution 3-D reservoir bathymetry results for the dynamic area over the last three decades. The bathymetry for the central reservoir area can be projected by extrapolation and then integrated with the remotely sensed results to obtain the full bathymetry. The highlight is that a 30-m resolution and high-quality bathymetry profile representing the complete range of the dynamic reservoir area over more than 30 years (i.e., 58% of Lake Mead’s capacity) was produced exclusively from remote sensing data.

Until now, there has been no cost-effective approach to derive reservoir bathymetry on a global scale. This approach was motivated by a need to fill in this gap and to eventually lead to a global bathymetry product suitable for applications across disciplines. It can be immediately usable once the ICESat-2 ATLAS data become available.

## ACKNOWLEDGMENT

The resultant bathymetry for Lake Mead in this study is available through the Land Surface Hydrology Research Group’s website at Texas A&M University, College Station, TX, USA, (<https://ceprofs.civil.tamu.edu/hgao/>). The authors would like to thank L. Brekke, A. Danner, and K. Nowak from the United States Bureau of Reclamation (USBR), for providing the survey lidar data. This work has benefitted from the usage of the Texas A&M Supercomputing Facility (<http://sc.tamu.edu>). They would also like to thank Dr. K.-H. Tseng at National Central University, Taoyuan City, Taiwan, for sharing the bathymetry projection algorithm. Analyses of MABEL data were supported by the NASA Cryosphere Program and through the ICESat-2 Project Office.

## REFERENCES

- [1] A. J. Heathcote, P. A. del Giorgio, and Y. T. Prairie, “Predicting bathymetric features of lakes from the topography of their surrounding landscape,” *Can. J. Fisheries Aquatic Sci.*, vol. 72, pp. 643–650, May 2015.
- [2] V. Mishra, K. A. Cherkauer, and L. C. Bowling, “Parameterization of lakes and wetlands for energy and water balance studies in the great lakes region,” *J. Hydrometeorol.*, vol. 11, no. 5, pp. 1057–1082, 2010.
- [3] I. N. Mohammed and D. G. Tarboton, “On the interaction between bathymetry and climate in the system dynamics and preferred levels of the Great Salt Lake,” *Water Resour. Res.*, vol. 47, pp. 1–15, Feb. 2011.
- [4] E. Dutra *et al.*, “An improved snow scheme for the ECMWF land surface model: Description and offline validation,” *J. Hydrometeorol.*, vol. 11, no. 4, pp. 899–916, 2010.
- [5] W. R. Rouse *et al.*, “The role of northern lakes in a regional energy balance,” *J. Hydrometeorol.*, vol. 6, no. 3, pp. 291–305, 2005.

- [6] P. Samuelsson, E. Kourzeneva, and D. Mironov, "The impact of lakes on the European climate as simulated by a regional climate model," *Boreal Environ. Res.*, vol. 15, no. 2, pp. 113–129, 2010.
- [7] B. Lehner and P. Döll, "Development and validation of a global database of lakes, reservoirs and wetlands," *J. Hydrol.*, vol. 296, nos. 1–4, pp. 1–22, Aug. 2004.
- [8] G. Balsamo, R. Salgado, E. Dutra, S. Boussetta, T. Stockdale, and M. Potes, "On the contribution of lakes in predicting near-surface temperature in a global weather forecasting model," *Tellus A, Dyn. Meteorol. Oceanogr.*, vol. 64, no. 1, 2012, Art. no. 15829.
- [9] J.-F. Pekel, A. Cottam, N. Gorelick, and A. S. Belward, "High-resolution mapping of global surface water and its long-term changes," *Nature*, vol. 540, pp. 418–422, Dec. 2016.
- [10] B. F. Chao, Y. H. Wu, and Y. S. Li, "Impact of artificial reservoir water impoundment on global sea level," *Science*, vol. 320, no. 5873, pp. 212–214, 2008.
- [11] B. Lehner *et al.*, *Global Reservoir and Dam Database, Version 1 (GRanDv1): Dams, Revision 01*. Palisades, NY, USA: NASA Socioeconomic Data and Applications Center (SEDAC), 2011.
- [12] D. P. Lettenmaier and P. Milly, "Land waters and sea level," *Nature Geosci.*, vol. 2, pp. 452–454, Jul. 2009.
- [13] C. Nilsson, C. A. Reidy, M. Dynesius, and C. Revenga, "Fragmentation and flow regulation of the world's large river systems," *Science*, vol. 308, no. 5720, pp. 405–408, 2005.
- [14] P. Döll, K. Fiedler, and J. Zhang, "Global-scale analysis of river flow alterations due to water withdrawals and reservoirs," *Hydrol. Earth Syst. Sci.*, vol. 13, pp. 2413–2432, Dec. 2009.
- [15] I. Haddeland, T. Skaugen, and D. P. Lettenmaier, "Anthropogenic impacts on continental surface water fluxes," *Geophys. Res. Lett.*, vol. 33, no. 8, pp. 1–4, 2006.
- [16] N. Hanasaki, S. Kanae, and T. Oki, "A reservoir operation scheme for global river routing models," *J. Hydrol.*, vol. 327, pp. 22–41, Jul. 2006.
- [17] N. Voisin *et al.*, "Effects of spatially distributed sectoral water management on the redistribution of water resources in an integrated water model," *Water Resour. Res.*, vol. 53, pp. 4253–4270, May 2017.
- [18] T. Zhou, B. Nijssen, H. Gao, and D. P. Lettenmaier, "The contribution of reservoirs to global land surface water storage variations," *J. Hydrometeorol.*, vol. 17, no. 1, pp. 309–325, 2016.
- [19] Z. Zajac, B. Revilla-Romero, P. Salamon, P. Burek, F. A. Hirpa, and H. Beck, "The impact of lake and reservoir parameterization on global streamflow simulation," *J. Hydrol.*, vol. 548, pp. 552–568, May 2017.
- [20] B. Hell, B. Broman, L. Jakobsson, M. Jakobsson, Å. Magnusson, and P. Wiberg, "The use of bathymetric data in society and science: A review from the Baltic Sea," *Ambio*, vol. 41, pp. 138–150, Mar. 2012.
- [21] M. L. Messager, B. Lehner, G. Grill, I. Nedeva, and O. Schmitt, "Estimating the volume and age of water stored in global lakes using a geostatistical approach," *Nature Commun.*, vol. 7, Dec. 2016, Art. no. 13603.
- [22] J. Gao, "Bathymetric mapping by means of remote sensing: Methods, accuracy and limitations," *Prog. Phys. Geogr.*, vol. 33, pp. 103–116, Feb. 2009.
- [23] B. K. Odhiambo and S. K. Boss, "Integrated echo sounder, GPS, and GIS for Reservoir sedimentation studies: Examples from two Arkansas lakes," *J. Amer. Water Resour. Assoc.*, vol. 40, no. 4, pp. 981–997, 2004.
- [24] R. C. Hilldale and D. Raff, "Assessing the ability of airborne LiDAR to map river bathymetry," *Earth Surf. Processes Landforms*, vol. 33, pp. 773–783, Apr. 2008.
- [25] K. Saylam, R. A. Brown, and J. R. Hupp, "Assessment of depth and turbidity with airborne Lidar bathymetry and multiband satellite imagery in shallow water bodies of the Alaskan North Slope," *Int. J. Appl. Earth Observ. Geoinf.*, vol. 58, pp. 191–200, Jun. 2017.
- [26] C.-K. Wang and W. D. Philpot, "Using airborne bathymetric lidar to detect bottom type variation in shallow waters," *Remote Sens. Environ.*, vol. 106, pp. 123–135, Jan. 2007.
- [27] C. Amante. (2009). *ETOPO1 1 Arc-Minute Global Relief Model: Procedures, Data Sources and Analysis*. [Online]. Available: <http://www.ngdc.noaa.gov/mgg/global/global.html>
- [28] E. Kourzeneva, H. Asensio, E. Martin, and S. Faroux, "Global gridded dataset of lake coverage and lake depth for use in numerical weather prediction and climate modelling," *Tellus A, Dyn. Meteorol. Oceanogr.*, vol. 64, Dec. 2012, Art. no. 15640.
- [29] W. Yigzaw *et al.*, "A new global storage-area-depth data set for modeling reservoirs in land surface and Earth system models," *Water Resour. Res.*, vol. 54, pp. 10372–10386, Dec. 2018.
- [30] K.-H. Tseng, C. K. Shum, J.-W. Kim, X. Wang, K. Zhu, and X. Cheng, "Integrating Landsat imageries and digital elevation models to infer water level change in Hoover Dam," *IEEE J. Sel. Topics Appl. Earth Observ. Remote Sens.*, vol. 9, no. 4, pp. 1696–1709, Apr. 2016.
- [31] J.-F. Crétaux *et al.*, "SOLS: A lake database to monitor in the Near Real Time water level and storage variations from remote sensing data," *Adv. Space Res.*, vol. 47, pp. 1497–1507, May 2011.
- [32] J.-F. Crétaux *et al.*, "Lake volume monitoring from space," *Surv. Geophys.*, vol. 37, pp. 269–305, Mar. 2016.
- [33] G. Zhang *et al.*, "Lake volume and groundwater storage variations in Tibetan Plateau's endorheic basin," *Geophys. Res. Lett.*, vol. 44, pp. 5550–5560, Jun. 2017.
- [34] A. Getirana, H. C. Jung, and K.-H. Tseng, "Deriving three dimensional reservoir bathymetry from multi-satellite datasets," *Remote Sens. Environ.*, vol. 217, pp. 366–374, Nov. 2018.
- [35] H. Gao, "Satellite remote sensing of large lakes and reservoirs: From elevation and area to storage," *Wiley Interdiscipl. Rev., Water*, vol. 2, no. 2, pp. 147–157, 2015.
- [36] V. H. Phan, R. Lindenbergh, and M. Menenti, "ICESat derived elevation changes of Tibetan lakes between 2003 and 2009," *Int. J. Appl. Earth Observ. Geoinf.*, vol. 17, pp. 12–22, Jul. 2012.
- [37] G. Zhang, H. Xie, S. Kang, D. Yi, and S. F. Ackley, "Monitoring lake level changes on the Tibetan Plateau using ICESat altimetry data (2003–2009)," *Remote Sens. Environ.*, vol. 115, pp. 1733–1742, Jul. 2011.
- [38] S. Zhang, H. Gao, and B. S. Naz, "Monitoring reservoir storage in South Asia from multisatellite remote sensing," *Water Resour. Res.*, vol. 50, no. 11, pp. 8927–8943, 2014.
- [39] M. F. Jasinski, J. D. Stoll, W. B. Cook, M. Ondrusk, E. Stengel, and K. Brunt, "Inland and near-shore water profiles derived from the high-altitude Multiple Altimeter Beam Experimental Lidar (MABEL)," *J. Coastal Res.*, vol. 76, pp. 44–55, Dec. 2016.
- [40] L. Yang, X. Meng, and X. Zhang, "SRTM DEM and its application advances," *Int. J. Remote Sens.*, vol. 32, no. 14, pp. 3875–3896, 2011.
- [41] J. E. Bailey, S. Self, L. K. Wooller, and P. J. Mouginis-Mark, "Discrimination of fluvial and eolian features on large ignimbrite sheets around La Pacana Caldera, Chile, using Landsat and SRTM-derived DEM," *Remote Sens. Environ.*, vol. 108, pp. 24–41, May 2007.
- [42] R. Wright, H. Garbeil, S. M. Baloga, and P. J. Mouginis-Mark, "An assessment of shuttle radar topography mission digital elevation data for studies of volcano morphology," *Remote Sens. Environ.*, vol. 105, pp. 41–53, Nov. 2006.
- [43] D. Yamazaki *et al.*, "Loughlin, J. C. Neal, "A high-accuracy map of global terrain elevations," *Geophys. Res. Lett.*, vol. 44, pp. 5844–5853, Jun. 2017.
- [44] United States Bureau of Reclamation (USBR). (2011). *2009 Lake Mead LiDAR Survey* <https://www.usbr.gov/lc/region/g2000/2009MeadLIDARsurvey.pdf>
- [45] G. Zhao and H. Gao, "Automatic correction of contaminated images for assessment of reservoir surface area dynamics," *Geophys. Res. Lett.*, vol. 45, pp. 6092–6099, Jun. 2018.
- [46] A. M. Melesse and J. D. Jordan, "A comparison of fuzzy vs. augmented-ISODATA classification algorithms for cloud-shadow discrimination from Landsat images," *Photogramm. Eng. Remote Sens.*, vol. 68, pp. 905–911, Sep. 2002.
- [47] C. Ren, C. Li, K. Jia, S. Zhang, W. Li, and Y. Cao, "Water quality assessment for Ulansuhai Lake using fuzzy clustering and pattern recognition," *Chin. J. Oceanol. Limnol.*, vol. 26, pp. 339–344, Aug. 2008.
- [48] S. K. Mcfeeter, "The use of the normalized difference water index (NDWI) in the delineation of open water features," *Int. J. Remote Sens.*, vol. 17, no. 7, pp. 1425–1432, 1996.
- [49] J. Li and Y. Sheng, "An automated scheme for glacial lake dynamics mapping using Landsat imagery and digital elevation models: A case study in the Himalayas," *Int. J. remote Sens.*, vol. 33, pp. 5194–5213, 2012.
- [50] G. Zhang, G. Zheng, Y. Gao, Y. Xiang, Y. Lei, and J. Li, "Automated water classification in the Tibetan plateau using Chinese GF-1 WVF data," *Photogramm. Eng. Remote Sens.*, vol. 83, pp. 509–519, Jul. 2017.
- [51] H. Gao, C. Birkett, and D. P. Lettenmaier, "Global monitoring of large reservoir storage from satellite remote sensing," *Water Resour. Res.*, vol. 48, no. 9, pp. 1–12, 2012.
- [52] United States Bureau of Reclamation. (2008). *2001 Lake Mead Sedimentation Survey*. [Online]. Available: <https://www.usbr.gov/tscl/techreferences/reservoir/2001%20Lake%20Mead%20Sedimentation%20Survey.pdf>

- [53] T. Markus *et al.*, “The Ice, Cloud, and land Elevation Satellite-2 (ICESat-2): Science requirements, concept, and implementation,” *Remote Sens. Environ.*, vol. 190, pp. 260–273, Mar. 2017.
- [54] Y. Li, H. Gao, M. F. Jasinski, S. Zhang, and J. D. Stoll, “Comparing storage estimations for Lake Mead using multi-source satellite altimetry and imagery data,” presented at the AGU Fall Meeting, New Orleans, LA, USA, Dec. 2017.
- [55] Z. Duan and W. G. M. Bastiaanssen, “Estimating water volume variations in lakes and reservoirs from four operational satellite altimetry databases and satellite imagery data,” *Remote Sens. Environ.*, vol. 134, pp. 403–416, Jul. 2013.
- [56] M. Moknatian, M. Piasecki, and J. Gonzalez, “Development of geospatial and temporal characteristics for hispaniola’s lake azuei and enriquillo using Landsat imagery,” *Remote Sens.*, vol. 9, no. 6, p. 510, 2017.
- [57] G. Zhao, H. Gao, B. S. Naz, S.-C. Kao, and N. Voisin, “Integrating a reservoir regulation scheme into a spatially distributed hydrological model,” *Adv. Water Resour.*, vol. 98, pp. 16–31, Dec. 2016.



**Yao Li** received the B.Sc. degree in geographic information systems from the China University of Geosciences, Beijing, China, in 2012. He is currently pursuing the Ph.D. degree with the Environmental & Water Resources Engineering Group, Department of Civil and Environmental Engineering, Texas A&M University, College Station, TX, USA.

His research interests include the remote sensing of inland water and ocean color.



**Huilin Gao** (S’04–M’05–SM’17) received the B.S. and M.S. degrees in atmospheric sciences from Peking University, Beijing, China, in 1997 and 2000, respectively, and the Ph.D. degree in civil and environmental engineering from Princeton University, Princeton, NJ, USA, in 2005.

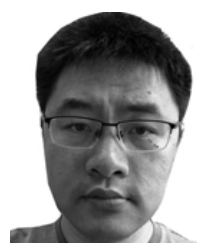
From 2005 to 2007, she was a Research Faculty with the School of Earth and Atmospheric Sciences, Georgia Institute of Technology, Atlanta, GA, USA. From 2008 to 2012, she was a Research Associate of civil and environmental engineering with the University of Washington, Seattle, WA, USA. Since 2012, she has been an Associate Professor with the Civil and Environmental Engineering Department, Texas A&M University, College Station, TX, USA. Her research interests include hydrologic monitoring and prediction, climate change, land cover land use change, water resources management, and satellite remote sensing in hydrology.

Dr. Gao was a recipient of the CAREER Award from the Environmental Sustainability Program of the National Science Foundation in 2015 and the Gulf Research Program Early-Career Research Fellowship from the National Academy of Sciences, Engineering, and Medicine, in 2016.



**Michael F. Jasinski** was born in Syracuse, NY, USA, in 1952. He received the B.S. degree in civil and environmental engineering and the M.S. degree in hydrology from Cornell University, Ithaca, NY, USA, in 1974 and 1976, respectively, and the Sc.D. degree in hydrology from the Massachusetts Institute of Technology, Cambridge, MA, USA, in 1989.

From 1978 to 1984, he was a Water Resources Engineer with Harza Engineering Company, Chicago, IL, USA. Since 1989, he has been a Research Scientist with the Hydrological Sciences Laboratory, NASA Goddard Space Flight Center, Greenbelt, MD, USA, where he is involved in satellite remote sensing of terrestrial physics. He is currently the Lead Hydrologist for the NASA ICESat-2 Mission, including the Lead Developer of its inland water height retrieval algorithm.



**Shuai Zhang** received the B.S. degree in surveying from Southeast University, Nanjing, China, in 2008, the M.S. degree in geography information engineering from Wuhan University, Wuhan, China, in 2012, and the Ph.D. degree in civil engineering from Texas A&M University, College Station, TX, USA, in 2017.

Since 2017, he has been a Post-Doctoral Scholar with the Department of Geological Sciences, The University of North Carolina at Chapel Hill, Chapel Hill, NC, USA. His research interests include satellite remote sensing in hydrology, lake ice phenology in the Arctic, and machine learning.



**Jeremy D. Stoll** received the B.S.E. degree in civil and environmental engineering from Duke University, Durham, NC, USA, in 1998, and the M.E. degree in water resources engineering from the University of Maryland, College Park, MD, USA, in 2001.

Since 1998, he has been with the Hydrological Sciences Laboratory, NASA Goddard Space Flight Center, Greenbelt, MD, USA, and also with Science Systems and Applications, Inc., Lanham, MD, USA. He was involved in hydrologic research and water surface remote sensing algorithm development. His research interests include satellite remote sensing in hydrology, water resources management, and hydrologic modeling.